This article has been accepted for publication in IEEE Journal of Selected Topics in Applied Earth Observations and Remote Sensing. This is the author's version which has not been fully edited and content may change prior to final publication. Citation information: DOI 10.1109/JSTARS.2025.3628450

Optimizing change detection methods for flood mapping using polarimetric SAR

Isundwa K. Felix, *Student Member, IEEE,* Marino Armando, *Member, IEEE,* Andrea Berardi, Isabella Bovolo, Peter Hunter, Claire Neil, Cristian Silva Perez, and Thiago S. F. Silva

***Abstract*—Flooding is becoming increasingly frequent and severe worldwide, posing significant risks to lives and property. Accurate flood information, particularly regarding its extent and location, is essential for effective mitigation efforts. This study examines the May 2023 Emilia-Romagna flood in Italy to enhance flood detection accuracy. For the first time, we applied optimization of power difference and ratio polarimetric change detection methods to identify the most effective flood detection method. Additionally, we tested various reference images within a time series to determine the most suitable reference image using Sentinel-1 Synthetic Aperture Radar data spanning from 2017 to 2023. Results revealed that the Optimisation of Power Ratio (OPRatio) method was most effective in detecting flooded areas. Notably, we established that in the study area, the optimal reference image is not always the one immediately preceding the flood; instead, an image acquired a month before flood or a composite of images from March across multiple years provided the most accurate results. This approach, combined with the OPRatio detector, achieved the highest accuracy and lowest false alarm rates. When applied to a flood event in Scotland, it similarly reduced false detections. This study underscores the importance of employing polarimetric change detectors alongside optimal reference images to improve the precision and reliability of flood mapping.**

***Index Terms*—Change detection, SAR Polarimetry, Flood mapping, Reference image selection, Sentinel-1, Polarimetric flood mapping**

I. Introduction

THIS article presents the application of SAR based polarimetric change detection methods for open flood mapping and the determination of the best reference image using time series data. Floods are natural disasters that cause widespread destruction of property and loss of life. They lead to contamination of water sources resulting in water-borne diseases, agricultural losses, and damages to livelihoods, affecting large numbers of people, especially in dense population centres [1]. Daily extreme rainfall rates have been intensifying globally throughout the 20th and 21st century [2] increasing the probability of flooding in many catchments [3]. The increase in severity and frequency of flooding impacts local populations and affects critical infrastructure. Flood mapping is thus an important exercise in assessing the damages resulting from flooding and for organising relief efforts and can be used as a planning and regulatory tool to help identify areas with low flood risk for construction of infrastructure. However, the accuracy of flood maps depends on the method used and input datasets [4]. Flood mapping using remote sensing techniques are valuable in large scale mapping exercises and offer rapid assessment [5]. Remote sensing has also been identified as a significant tool in supporting flood preparedness, mitigation and recovery from flood disaster as described in the NASA Global Flood Mapping System [6].

Recent studies have demonstrated the application and effectiveness of flood mapping using remote sensing. Optical data from Landsat 5, 7, and 8 have been used in mapping flood extents achieving strong correlation with ground measurements [7]–[9]. Li *et al.* [10] combined low earth orbiting (LEO) and geostationary (GEO) satellite imagery to develop a global flood mapping system, with Landsat 8 OLI and validated using Sentinel-2 imagery. Senitinel-2 data has been used in flood mapping by applying different machine learning techniques such as deep convolutional neural network [11], random forests [12], support vector regression and hyperparameterisation in susceptibility mapping [13]. Indices such as Normalized difference vegetation index (NDVI), Normalized Difference Water Index (NDWI), Modified Normalized Difference Water Index (MNDWI) and Normalized Difference Pond Index (NDPI) have been applied in extracting water features [14]. Although these methods have been accurate in delineating flood and water extents, optical data which is affected by cloud cover and can only be acquired during day light hours, cannot detect floods under dense vegetation cover. In some cases, distinguishing between permanent and flood water is a challenge [15].

Synthetic Aperture Radar (SAR) which can collect data at any time of day, any weather conditions is an alternative source of data for flood mapping. Despite this advantage, interpretation, and extraction of valuable information from SAR is complex, complicated further by speckle noise in the data [16]. Where floods occur under vegetation and in an urban environment, extraction of flood surface is further complicated by the double-bounce effect due to the side looking nature of SAR and the vertical orientation of buildings and vegetation [17]. Flood extent from a SAR image can be extracted by classification using supervised and unsupervised classification, thresholding of backscatter intensity, or change detection [18]. SAR based thresholding of single flood images was found to

Isundwa K. Felix, Marino Armando, Peter Hunter, and Thiago S. F. Silva are with the Faculty of Natural Sciences, University of Stirling, Stirling, FK9 4LA, United Kingdom (e-mail: f.k.isundwa@stir.ac.uk).

Andrea Berardi is with the Faculty of Science, Technology, Engineering & Mathematics, The Open University, Milton Keynes, MK7 6AA, United Kingdom.

Isabella Bovolo is with the Department of Geography, Durham University, The Palatine Centre, Durham, DH1 3LE, United Kingdom.

Claire Neil is with the Scottish Environment Protection Agency, Strathallan House, Stirling, FK9 4TZ, United Kingdom.

Cristian Silva Perez is with Keen AI, Alcester Road, Birmingham, B13 8JP, United Kingdom.

Manuscript received April 19, 2021; revised August 16, 2021.

This work is licensed under a Creative Commons Attribution 4.0 License. For more information, see https://creativecommons.org/licenses/by/4.0/

This article has been accepted for publication in IEEE Journal of Selected Topics in Applied Earth Observations and Remote Sensing. This is the author's version which has not been fully edited and content may change prior to final publication. Citation information: DOI 10.1109/JSTARS.2025.3628450

be robust in separating flood and non-flood areas, however, the effect of radar shadow lowers the accuracy of detection [18]. Known thresholding methods such as Otsu [19], KI [20] either over-predicted or under-predicted the flooded areas when applied on a single image. These methods are influenced by the type of the probability distribution of the data. Change detection on the other hand reduces the need for additional data or processing [21] to eliminate shadows or existing water bodies while offering improved accuracy when combined with thresholding.

The selection of a reference image for change detection has been flagged as a potential cause of misclassification when selected mostly as a single image right before floods [18]. Li *et al.* [22] applied the Jensen-Shannon (JS) divergence-based index to select the reference image, which enabled selection of the best image from a series of images. Zhao *et al.* [23] applied an index to automatically select the reference image by measuring the Euclidean distance between two Gaussian distributions to measure the similarity between reference image and the flood image. Despite the applied methods, significant false alarms were recorded from the result and post-processing steps were applied to reduce the false alarms. Besides the choice of reference image and the detection method, the choice of input data influences the accuracy of results. There was observed difference in the results when *VV* polarisation (vertical transmit and vertical received), *HH* (horizontal transmit and horizontal received) and *VH* are compared [24]. Manavalan *et al.* [25] and [24] established that *VV* polarisation was effective at mapping partially submerged features. Different performance was recorded where the *VH* data gave the best detection accuracy [26], [27]. In general, studies have shown that polarimetric data usage have better performance especially in complex environments such as urban areas [28], [29]. The use of polarimetric data enables understanding of the scattering mechanism occurring in a scene. When fully polarimetric data is present, it enables full characterization of the scattering mechanism thus improving the accuracy of classification or target detection. However, this data is not readily available, and its access is costly. Sentinel-1 SAR data, which can not fully characterise the scattering mechanism (SM), is freely available and currently has 6 days repeat cycle enabling timeseries analysis.

Sentinel-1 data has been used in operational flood mapping such as the Copernicus Emergency Management Service (CEMS) which continuously monitors floods by integrating three flood mapping algorithms to enhance accuracy. Pixels are classified as flood if at least two algorithms identify the pixel as flooded [30]–[32]. The three algorithms include post-processing steps to improve the accuracy of the detection using features such as Height Above Nearest Drainage (HAND) index. These methods use backscatter intensity only. As established from previous research, the data, the reference image and the change detection method all together influence the accuracy of flood mapping. A common practice in flood mapping using changed detection methods has been to select the last image before a flood as a reference image. However, the selection of this reference image has been identified as a source of uncertainty leading to over-prediction or under-prediction of flooded areas. Considering the above, there is need to have flood detection method that gives the highest accuracy, least false alarms while offering reduced post-processing steps. Since the existing literature identified reference images as potential source of uncertainty, there is need to reduce this potential source of uncertainty. Apart from the reference image, the type of data has been identified as source of uncertainty in flood mapping, therefore there is need to utilise addition information stored in Sentinel-1 polarimetric data to improve flood detection.

In this study, we are presenting for the first time, the application of polarimetric-SAR change detectors for flood mapping. We present the application of the Optimisation of Power Difference (OPDiff) and Optimisation of Power Ratio (OPRatio) polarimetric change detection methods in mapping open flood areas. Similarly, we present a practical reference image selection strategy where, for the first time, all combinations of historical reference images (over 5 years of SAR data) were assessed to determine the optimal reference image. Furthermore, we propose a practical approach to reduce false alarms in flood mapping by combining the most suitable polarimetric change detection method with the optimal reference image.

II. Materials and Methods

A. Test Sites

1) Test Site 1: Imola: The test site selected in this research is the Emilia-Romagna region in Italy (Fig. 1). In May 2023, the Emilia-Romagna region was impacted by flooding caused by heavy rainfall. As of 2023-05-23, the Monte Albano rain gauge had recorded precipitation amounts of 261.2 mm between 2023-05-15 and 2023-05-17. This resulted in flooding in Bologna, Imola, and other southeast regions along the Adriatic Sea. The flooding resulted in the displacement of up to 13,000 people, 13 fatalities and property losses [33]. This region is prone to annual flooding from pluvial and fluvial causes.

2) Test Site 2: Forth Catchment, Scotland: Forth catchment is in central Scotland and is drained by the river Forth. The catchment is prone to annual flooding from precipitation causing rivers to bust their banks. Here, a flood occurred on 2023-10-08 along two tributaries (river Teith and Forth). The flood was a result of heavy rainfall with a two-day (2023-10-06 to 2023-10-07) average recorded rainfall of over 150 mm. During these two days, the average rainfall over the entire Scotland was recorded to be 64.1 mm amount which is considered the wettest two-day period on record since the 1891 [34]. Sentinel-1 acquired data on the day of flooding.

B. Data

1) SAR Data: Sentinel-1 C-band Single Look Complex(SLC) level 1 radar data was used in this study. The data analysed were historical Interferometric Wide (IW) products that were acquired over the study area between 2017 and 2023. Detailed documentation on the processing algorithms and steps are detailed in the product definition document [35]. There are three satellite passes over the area of interest along three different orbits (paths) and frame. These three passes covered

This work is licensed under a Creative Commons Attribution 4.0 License. For more information, see https://creativecommons.org/licenses/by/4.0/

This article has been accepted for publication in IEEE Journal of Selected Topics in Applied Earth Observations and Remote Sensing. This is the author's version which has not been fully edited and content may change prior to final publication. Citation information: DOI 10.1109/JSTARS.2025.3628450

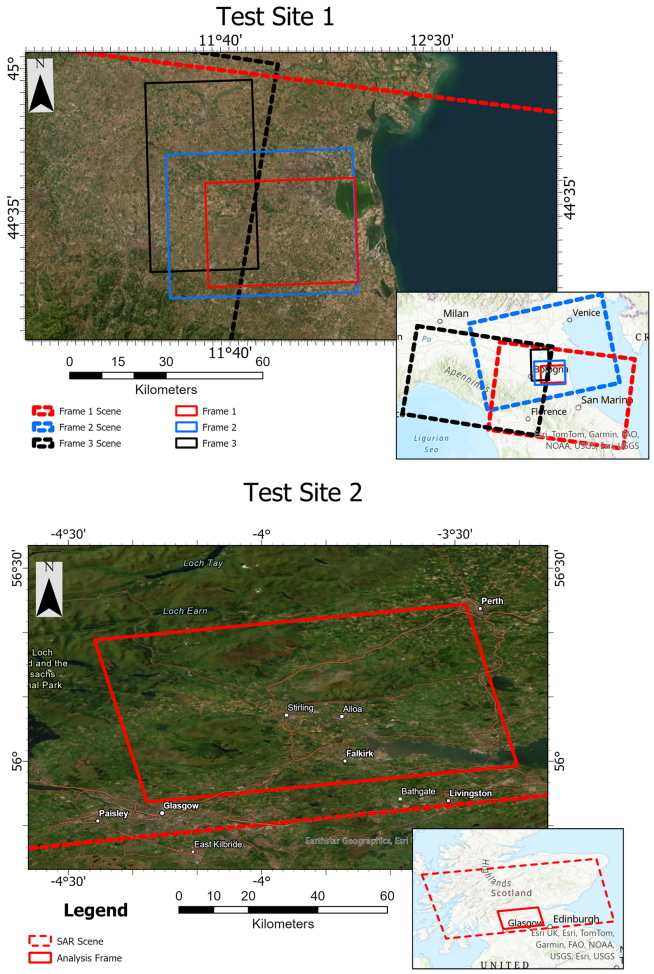

Fig. 1. Test Site 1: The Imola study area (Emilia-Romagna, Italy) and the coverage of Sentinel-1 C-band SAR datasets, acquired between 2017 and 2023, representing three satellite passes along three different orbits (see Table 1). Test Site 2: Forth river catchment in Scotland Sentinel-1 coverage. The dashed polygons represent the entire SAR scene while the continuous lines represent selected areas for analysis from the scene.

the area of interest on different dates and different incident angles. These three different coverages of the area of interest were analysed separately and here are referred to as 'frames', as described in the table I. Data in frames 1 and 2 were used for identifying the best reference image and detector while the frame 3 was used for test these findings further. The data SLC have two channels, *VV* and *VH*. The data acquired over Imola was used to optimise the detection methods, and select the reference image while the Forth flood event data was used for comparison with existing products from CEMS.

2) Optical Data: PlanetScope optical data acquired by the PSB.SD sensor (SuperDoves) onboard SkySats satellites were used in assessing the accuracy of the tested detectors. This 3rd generation instrument has 8 bands (Coastal Blue 431-452 nm, Blue: 465-515 nm, Green I: 513. - 549 nm, Green: 547. - 583 nm, Yellow: 600-620 nm, Red: 650 - 680 nm, Red-Edge: 697 - 713 nm, and NIR: 845 - 885 nm). Blue, green, red and Near Infra-red bands were used in this research [36] The data have a resolution of 3 m and were acquired on the same day as Sentinel-1 satellites.

TABLE I
TABLE OF SAR DATASETS USED IN THE ANALYSIS IN IMOLA, ITALY AND FORTH CATCHMENT, SCOTLAND. ASC. REPRESENTS DATA ACQUIRED IN ASCENDING ORBIT WHILE DES. IS DESCENDING ORBIT

Region	Frame	Orbit	Path (frame)	No. of Images	Product	Swath/ Sub-Swath	Incidence angle
Imola	Frame 1	Des.	95 (445)	180	SLC GRD	IW2/ 2-4	38.3^0
	Frame 2	Asc.	117 (143)	196	SLC GRD	IW2/ 1-4	38.3^0
	Frame 3	Des.	168 (444)	185	SLC GRD	IW1/ 1-4	32.9^0
Forth	Frame 1	Asc.	30 (182)	18	SLC GRD	IW2/ 1-4	38.3^0

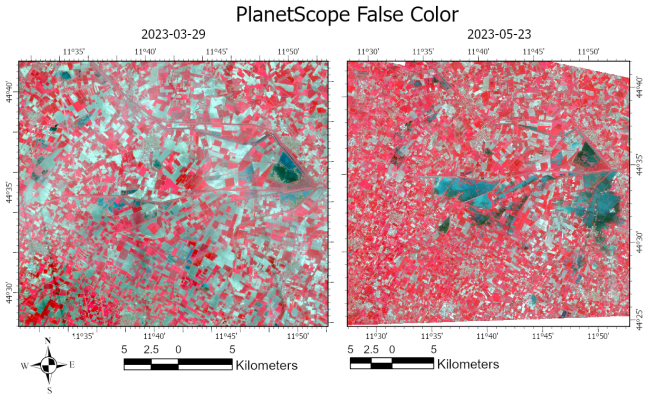

Fig. 2. PlanetScope images before (2023-03-29) and during flood (22-05-2023) event. Image © 2023 Planet Labs PBC

C. Data Analysis Approach

We applied a timeseries approach to determine the best change detection method for mapping open floods and the best reference image. To achieve this, the analysis of the data followed the following steps:

- Pre-processing of all historical SAR data
- Creation of flood and no-flood area masks from optical data to be used for accuracy assessment
- Selection of the reference image to be used in change detection
- Testing the different change detection methods
- For every reference image used, estimate the optimal parameters from the change detection results and assessing the accuracy
- Estimate the overall performance of each detector

The specific details carried-out in each step are discussed in the subsequent subsections.

1) SAR Data Processing: Pre-processing and co-registration processing steps were applied on the level-1 data prior to change detection. These two steps were batch processed using ESA SNAP Graph Processing Tool (GPT). The SLC pre-processing involved applying an orbit file, TOPSAR split, calibration, TOPSAR De-burst, generation of polarimetric matrices (Covariance Matrix), multi-looking, polarimetric speckle filtering, terrain correction, and sub-

This work is licensed under a Creative Commons Attribution 4.0 License. For more information, see https://creativecommons.org/licenses/by/4.0/

This article has been accepted for publication in IEEE Journal of Selected Topics in Applied Earth Observations and Remote Sensing. This is the author's version which has not been fully edited and content may change prior to final publication. Citation information: DOI 10.1109/JSTARS.2025.3628450

setting. The GRD data was generated from the SLC data after pre-processing. The pre-processing of the SLC data before change detection results to the dual-pol covariance matrix elements C_{11}, C_{22}, and C_{12} which correspond to the intensities of *VV*, *VH*, and the cross correlation between *VV* and *VH* (denoted as $VV \cdot VH^*$), respectively.

2) Flood and No-Flood Mask: On the dates when floods occurred, visually identified areas of flood and non-flood areas were manually digitised into polygon shapefiles from PlanetScope images with total area shown in table II. The digitised polygons were then rasterised into raster file with the same resolution and extent as the SAR data to ensure consistency during analysis. It is important to note that there may be slight over estimation or underestimation of flooded area pixels due to the difference in the acquisition times between SAR and optical data.

TABLE II
PLANETSCOPE DATA USED FOR GENERATING ACCURACY ASSESSMENTS. THE FLOODED AND NON-FLOODED AREAS ARE DIGITIZED POLYGONS FROM THE IMAGES.

Frame	Sentinel-1 date (time)	PlanetScope date (time)	Flooded Area (Ha)	Non-flooded (Ha)
Frame 1	2023-05-22 (05:19:44)	2023-05-22 (09:07:48)	3237.95	3,881.93
Frame 2	2023-05-23 (17:06:53)	2023-05-23 (09:48:22)	1682.47	2,740.35
Frame 3	2023-05-27 (05:27:54)	2023-05-27 (09:14:40)	491.76	2,436.30

3) Reference Image Selection: We applied all historical images as reference images in during change detection. This testing was done for Imola data only. This is to say, for frame 1 which had 180 images available on record (including the flood image) we used each individual image as reference excluding the flood image (2023-05-22) and performed change detection on the flood image. Therefore, there were 179 change detection results recorded as per the date of the reference image. This was repeated for Frame 2. For Scotland, the best reference image and change detection method identified from the test in Imola was used as will be established in subsequent sections.

4) Change Detection: Scattering mechanisms (SM) such as double bounce, surface, volume scattering or specular reflection occur in a natural environment depending on factors such as roughness, or dielectric constant [37]. In an area where there is open flooding, the scattering mechanism is mainly dominated by specular reflection. When two images are compared where one is acquired before a flood and one after/during a flood event, the one with floods will record a drop in backscatter intensity. If these were areas covered by vegetation before, there would be a removal of volume scattering and an introduction of specular scattering as shown in Fig. 3. Therefore, the analysis in this study aims at identifying areas that are dominated by specular reflection. Since the SM cannot be deterministically described, they are described using the covariance matrix $[C]$ [38]. The description is only possible using polarimetry by applying decompositions such as the Cloude-Pottier decomposition, which enables the

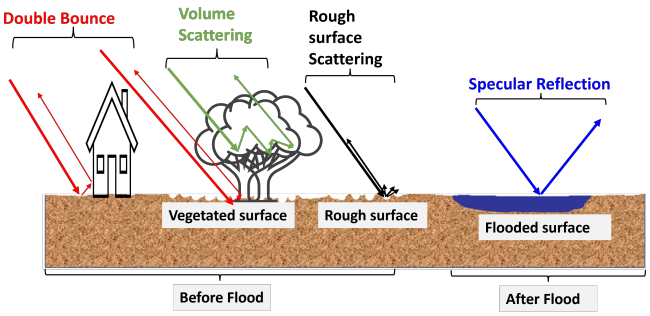

Fig. 3. Schematic image showing scattering mechanisms for an incident wave on different surfaces

inference of the SM occurring in a scene (eigenvectors) and the physical characteristics of the SM (eigenvalues) [38]. As in our case of floods, this would correspond to a drop in the scattering power(eigenvalues) between two dates. In this research, the polarimetric information stored in elements of the covariance matrix were used to identify flooded areas. Five change detection methods are tested and compared in time series. The Optimisation of Power Difference (OPDiff), Optimisation of Power Ratio (OPRatio), and difference in Cloude-Pottier eigenvalues were applied on polarimetric data while the difference and the ratio of *VV* or *VH* were applied on intensity data.

1) *Optimisation of Power Difference (OPDiff)*
The OPDiff is an additive model where the change matrix $[C_\Delta]$ is calculated by getting the difference between two covariance matrices $[C_1]$ and $[C_2]$ [39]. In the case of flood studies, the $[C_1]$ and $[C_2]$ matrices represent images acquired before and after(during) flooding respectively. The optimisation of the change matrix $[C_\Delta]$ enables the quantification of whether the power of the SM is increasing or decreasing. The quadratic form of Equation 1 is optimised using the Lagrangian optimisation to give minimum and maximum projection vectors.

$$\underline{\omega}^*[C_\Delta]\underline{\omega} \tag{1}$$

Equation 2 is a result of constraining $\underline{\omega}$ to be unitary, differentiating and setting the derivative equal to zero.

$$[C_\Delta]\underline{\omega} = \lambda\underline{\omega} \tag{2}$$

where $\underline{\omega}$ is the projection vector. A step-by-step derivation of the optimisation is detailed in [39]. The change matrix $[C_\Delta]$ is normal with real eigenvalues. However, these eigenvalues are not necessarily positive since they are result of either the increase or decrease in the power of the SM. The change matrix $[C_\Delta]$ contains two eigenvalues which will correspond to the difference between the maximum eigenvalues *(Diff1)* and minimum eigenvalues *(Diff2)*. Additionally, we investigate the performance when using the information stored in the eigenvectors. These eigenvectors are characterised by as set of alpha angles(α) which describe the dominant scattering mechanisms such that when $\alpha \approx 0^0$ surface

This work is licensed under a Creative Commons Attribution 4.0 License. For more information, see https://creativecommons.org/licenses/by/4.0/

This article has been accepted for publication in IEEE Journal of Selected Topics in Applied Earth Observations and Remote Sensing. This is the author's version which has not been fully edited and content may change prior to final publication. Citation information: DOI 10.1109/JSTARS.2025.3628450

scattering, $\alpha \approx 45^0$ for volume scattering and $\alpha \approx 90^0$ for double bounce. This is done by getting the product of the eigenvalues and the sine or cosine of the alpha angles. The two products are *Diff1*sin(alpha1)* and *Diff2*cos(alpha2)*. This is because the eigenvector contains physical information, and this may improve the detection.

2) *Optimisation of Power Ratio (OPRatio)*
OPRatio is a multiplicative change detection model. In this model, the optimisation is implemented by applying a constrained Lagrangian method that returns a diagonalization as in Equation 3.

$$[C_1]^{-1}[C_2]\underline{\omega} = \lambda\underline{\omega} \tag{3}$$

this results in projection vectors which suffer maximum/minimum changes and eigenvalues representing the maximum/minimum ratio between the power of that scattering mechanism. The change matrix $[C_r]$ in the OPRatio can be defined as in the Equation 4.

$$[C_r] = [C_1]^{-1}[C_2] \tag{4}$$

This change matrix can be diagonalised resulting in real positive eigenvalues. A step-by-step derivation of the optimisation is detailed in [40]. The change matrix $[C_r]$ is normal, and the resultant eigenvectors are not bound to be orthogonal. The eigenvalue lies between zero and infinity. The resulting eigenvalues will be referred to as *Rat1* and *Rat2* to represent the maximum and minimum eigenvalues respectively of this matrix.

3) *Cloude-Pottier Eigenvalues Difference*
This method estimates the difference between the eigenvalues generated after the decomposition of the covariance matrix as proposed by Cloude-Pottier [38]. Unlike the previous two models where optimisation was performed on a change matrix, here, eigenvalues are extracted directly from $[C_1]$ and $[C_2]$ before getting their difference. The eigenvalues generated for the covariance matrix for the date before floods are referred to λ_1^{max} and λ_1^{min}. Similarly, two eigenvalues generated from the dates with floods are referred to as λ_2^{max} and λ_2^{min}. Afterwards, the maximum/minimum eigenvalue from the first date are subtracted from corresponding maximum/minimum eigenvalue of the second date as shown in Equation 5 and 6.

$$\lambda_{diff1} = {\lambda_1}^{max} - {\lambda_2}^{max} \tag{5}$$

$$\lambda_{diff2} = {\lambda_1}^{min} - {\lambda_2}^{min} \tag{6}$$

The difference from the maximum eigenvalue λ_{diff1} will be referred to as *LamD1* and the difference in the minimum eigenvalues λ_{diff2} as *LamD2*.

4) *Backscatter Intensity Difference and Ratio*
The difference and ratio between the intensity of radar backscatter between two dates can be used to estimate the flooded areas. The difference is calculated by subtracting data from corresponding polarisation between the two dates for polarization *VV* and *VH*. The ratios will be referred to as *RatVV* and *RatVH* while the difference as *DiffVV* and *DiffVH*.

5) Optimal Parameter Selection and Accuracy Assessment: The accuracy of using each reference image and methods were evaluated first using the Area under the curve (AUC) of the Receiver Operator Characteristic Curve and later by selecting optimal parameters that are threshold depended. A realistic classifier is not expected to have an AUC of less than 0.5 when a desired measure of prediction is close 1 [41]. To do this, minimum and maximum values were identified from each change detection results. An array of 1000 values was generated ranging from minimum and maximum values of the change detection results identified. Each value in the array was used as a threshold to separate the flood and no-flood areas. For each threshold value, the corresponding the probability of detection (PD), probability of false alarm (PF), F1-score, and accuracy were calculated by using the flood no-flood masks generated earlier from optical images. ROC curves were plotted for each date (result) and AUC calculated. Besides this, threshold depended optimal parameters from each detector and reference image was derived by selecting values that fulfil the following conditions: PD $>$ = 80% , PF $<$ = 10% and Accuracy $>$=80% where applicable. Afterwards, a single value threshold values that has the highest accuracy and least false alarm (PF) was selected. This process was repeated for 179 and 195 images in Frame 1 and Frame 2 respectively from Imola data. The results of this analysis were analysed using box-plots, ROC plots and tables as shown in the results section. The method is semi-supervised since we selected areas of flood and no-flood with optical data, but the procedure after that is automatic. This method is customised for this study to select optimal parameters only, other threshold selection methods can be applied besides this depending on the user needs.

6) Estimation of Detector Performance and Overall Performance: Since different detectors and reference will have different values in PD, PF, Accuracy, F1-score, and the overall measure of performance AUC. In an attempt to summarise this in a single metric, we propose the following overall performance. We combined all the derived performance indicators using Equation 7:

$$OP = \frac{(Accuracy + F1score + PD + (1 - PF) + AUC)}{n} \tag{7}$$

where n represents the number of parameters combined, in this case 5. This performance indicator has values from 0-1 where the least performing detector has 0 and the perfect detector has 1. Other linear combinations of performance indicators can be used based on user requirements, but here we use a simple scenario where all the indicators are weighted equally. It should be noted that unlike the AUC which is selected for a classifier on a certain reference image date, the other parameters (PD,PF, accuracy, F1-score) are selected at a single threshold value that gives the highest accuracy, PD and least PF.

7) Testing on Independent Dataset: After testing how different detectors and reference images performed from the analysis of Frame 1 and 2 from Imola, the best reference

This work is licensed under a Creative Commons Attribution 4.0 License. For more information, see https://creativecommons.org/licenses/by/4.0/

This article has been accepted for publication in IEEE Journal of Selected Topics in Applied Earth Observations and Remote Sensing. This is the author's version which has not been fully edited and content may change prior to final publication. Citation information: DOI 10.1109/JSTARS.2025.3628450

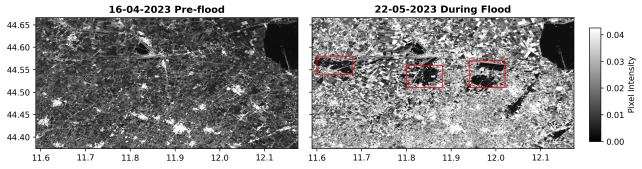

Fig. 4. Plot of C_{22} elements of the covariance matrix generated from the SLC. Image 1(left) was acquired 1 month before flooding while image 2 (right) is during flooding. Image 1 was used as the reference image for change detection. The two images are from Frame 1. Red rectangles depict flooded regions

image and highest performing detectors were applied on data from frame 3 and the accuracy assessed. Frame 3 flood image (2023-05-27) is from the same region as Frame 1 and 2 but has different acquisition characteristics from the other frames as shown in Table I. Besides testing with Imola data, the best detector was also applied to flood data acquired in Scotland as described in section II-A2 and visually compared to existing operational outputs applied in CEMS as shown in section III-H3.

III. Results

In the previous section, we described how polarimetric SAR data acquired in May 2023 in the Emilia-Romagna region during the flood period were processed to identify flood inundated areas. Three change detection methods were applied to the polarimetric data, while two were applied to the backscatter intensity only. The performance of each detection method was compared on a pixel-by-pixel basis against flood areas identified from optical data acquired on the same day as the SAR images. The section also outlined how multiple reference images were used with the aim of identifying which is the best for change detection. In this section, we present the result of the analysis on the different detectors and reference images.

A. Visual Inspection of Reference and Flood Image

We first visually inspected two images, acquired before (2023-04-16) and during floods (2023-05-22), to identify floods based on backscatter intensity (Fig. 4). The before flooding images have low backscatter in open water surfaces, while the flooding image shows additional areas with low backscatter which represent the flooded areas.

B. Evaluation of Detector Performance and reference image based on the AUC

The first step of the analysis was to assess the performance of the detectors by plotting the ROC curves for every reference images used, calculating the AUC and later getting the mean AUC for all reference image dates used for each detector as shown in Table III. Afterwards, we compared AUC of three reference images as shown in Fig. 5. When the mean AUC of frame 1 (mean of all images) is considered as shown in Table III, *Rat2* was the best detector closely followed by *Rat1*. *RatVH* and *RatVV* are the third and fourth best detectors. Two other detectors have values above 0.8 (*LamD2* and *DiffVH*). All other detectors have values below 0.8 as shown in Table III. When frame 2 is considered, almost similar performance is observed where the first two detectors are the same, the third and fourth detector are *RatVV* and *RatVH*. All other detectors had values below 0.8.

TABLE III
THESE RESULTS HAVE BEEN SORTED IN DESCENDING ORDER OF AUC OF FRAME 1. THE HIGHLIGHTED CELL COLOURS INDICATE THE BEST METRIC (GREEN) AND WORST METRIC (RED). COLUMNS REPRESENT MEAN VALUES AUC (AREA UNDER THE CURVE).

Mean Area Under the ROC curve (AUC)			
Rank	Detector	Frame 1	Frame 2
1	*Rat2*	0.930	0.853
2	*Rat1*	0.928	0.839
3	*RatVH*	0.904	0.802
4	*RatVV*	0.899	0.836
5	*LamD2*	0.843	0.738
6	*DiffVH*	0.831	0.729
7	*LamD1*	0.785	0.703
8	*DiffVV*	0.788	0.564
9	*Diff2*cos(alpha2)*	0.692	0.587
10	*Diff1*sin(alpha1)*	0.665	0.688
11	*Diff2*	0.611	0.430
11	*Diff1*	0.476	0.521

Reference image 2023-04-28: In frame 1, when the second last image before a flood is used as a reference and the AUC of the change detection is estimated, we note that *LamD2* is the best-ranked detector with an almost similar performance to *DiffVH*. *Rat2* and *Rat1* are third and fourth ranked while *Diff2*cos(alpha2)* is firth. The detectors *RatVH*, *RatVV*, and *LamD1* are sixth, seventh and eight with all the eighth detectors having AUC values over 0.9.

Reference image 2023-05-10: When the image before a flood in frame 1 was used as a reference, *Rat2* was the best detector followed by *Rat1*, *RatVH* and *LamD2* covering the first 4. Although the least AUC recorded was 0.627 from *Diff2*cos(alpha2)*, all detectors had lower AUC compared to the previous reference image and only four detectors had values of over 0.9. In summary, the two polarimetric detectors of *Rat2* and *Rat1* are generally highest ranked cumulatively. These are followed by two non-polarimetric ratio detectors *RatVH* and *RatVV*. However, when considering the second last image as reference, difference-based detectors (*LamD2* and *DiffVH*) have similar or better performance compared to *Rat2* and *Rat1*. Detectors with the highest AUC are recorded on 2023-04-28. The last image before floods doesn't have the highest AUC and most detectors are below 0.9 although the least has 0.6. Detectors *LamD1*, *DiffVV*, *Diff1*sin(alpha1)*, *Diff2*, *Diff1* are consistently poor detectors.

C. Estimating Threshold Depended Indicators of Detection Performance

In the preceding section, we presented results of analysis that was independent of thresholds used. In this section, we present the result of analysis based on thresholds that gave

This work is licensed under a Creative Commons Attribution 4.0 License. For more information, see https://creativecommons.org/licenses/by/4.0/

This article has been accepted for publication in IEEE Journal of Selected Topics in Applied Earth Observations and Remote Sensing. This is the author's version which has not been fully edited and content may change prior to final publication. Citation information: DOI 10.1109/JSTARS.2025.3628450

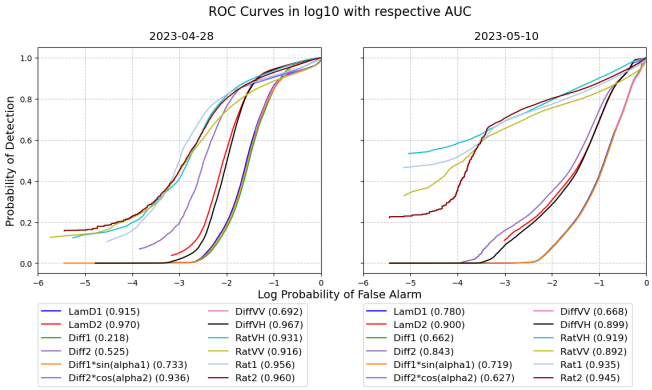

Fig. 5. Plot of ROC curve in PD against log PF for frame 1. The subplots represent the different dates of reference images acquired before flood where 2023-05-10 is the image before the flood image (2023-05-22), 2023-04-28 is the second image before a flood. For each date of plot, the AUC of each detector is calculated and displayed next to the detector on the legend.

the best parameters(highest accuracy and PD, and least PF). After estimating the best parameter for each reference date, we calculate and present the mean of all dates of reference image used as in Table IV.

TABLE IV
MEAN VALUES OF PERFORMANCE METRICS FOR THE DIFFERENT METHODS FROM ALL DATES ANALYSED. THE HIGHLIGHTED CELL COLOURS INDICATE THE BEST METRIC (GREEN) AND WORST METRIC (RED). COLUMNS REPRESENT MEAN VALUES AUC FOR EACH DETECTOR

Detector	Frame 1				Frame 2			
	PD	PF	Acc.	F1	PD	PF	Acc.	F1
Rat2	0.84	0.09	0.88	0.87	0.72	0.09	0.82	0.80
Rat1	0.85	0.10	0.87	0.87	0.72	0.14	0.79	0.78
RatVV	0.81	0.07	0.87	0.86	0.72	0.07	0.83	0.81
RatVH	0.86	0.14	0.86	0.86	0.74	0.20	0.77	0.77
Diff2	0.89	0.23	0.83	0.84	0.79	0.30	0.74	0.76
DiffVH	0.91	0.29	0.81	0.83	0.81	0.39	0.71	0.74
LamD2	0.92	0.29	0.81	0.83	0.81	0.36	0.72	0.75
Diff2 *cos(alpha2)	0.91	0.29	0.81	0.83	0.83	0.37	0.73	0.76
LamD1	0.84	0.31	0.76	0.78	0.73	0.32	0.71	0.71
*Diff1*sin(alpha1)	0.83	0.32	0.76	0.77	0.72	0.32	0.70	0.71
DiffVV	0.87	0.36	0.75	0.78	0.74	0.32	0.71	0.72
Diff1	0.83	0.32	0.75	0.77	0.73	0.32	0.70	0.71

Accuracy: Generally, polarimetric ratio based detectors *Rat2* and *Rat1* had higher accuracies followed by ratio based intensity detectors *RatVV* and *RatVH*. The difference based detectors had lower accuracies. This consistent for both frame 1 and 2. *DiffVV* was identified to be consistently poor. Analysing the two frames we can say that *Rat2*, *Rat1* and the two backscatter intensity ratios of *RatVV* and *RatVH* are the most accurate and *DiffVV* least accurate.

Rat1 had the highest accuracy score for Frame 1 followed by *Rat1*. The two backscattering intensity ratio detectors, *RatVV* and *RatVH*, are third and fourth respectively. In Frame 2, *RatVV* had the highest accuracy followed by *Rat2*. The third most accurate detector was *Rat1* followed by *RatVH*. The *Diff2*, and *Diff2*cos(alpha2)* are the fifth and sixth ranked detectors. Interestingly, from the table, the *DiffVV* had consistently low accuracy.

PD: Ratio based polarimetric detectors did not record the highest PD scores. The high PD scores were recorded by detectors *LamD2*, *Diff2*cos(alpha2)* and *DiffVH* in frame 1. Similar characteristic is observed in frame 2. In general, the detectors with high accuracies did not record high PD values.

PF: An interesting feature is identified when inspecting the PF scores. In this score, the ratio detectors record the least PF while the difference detectors have higher PF scores. *RatVV*, *Rat2* and *Rat1* have PF scores equal to or less than 10% in the two frames. *RatVH* has scores between 10% and 20%. All the other detectors had over 20% PF scores, a phenomenon evident in the two frames. From the analysis of the two frames, Analysing the PF of two frames, we can say that *RatVV*, *Rat2* and *Rat1* are the best detectors and *DiffVV* is the poorest. We can also say that the ratio-based detectors have lower PF rates than the difference-based detectors.

In summary, the results show that the ratio based polarimetric detector *Rat2* as the best detector. The ratio of backscatter intensities of *RatVV* is the second-best detector. *Rat1* and *RatVH* are third and fourth best detectors. The ratio-based detectors seem to be more robust than the difference. *DiffVH* has almost comparable accuracy but records higher PF rates. Interestingly, the *DiffVV* is consistently lowest ranked in most parameters. Therefore, detectors *DiffVV*, *LamD1*, *Diff1*sin(alpha1)*, and *Diff1* have been omitted from analysis in subsequent section due to poor performance.

D. Variability of Detection with Changing Reference

In the previous section, we presented the mean results of detectors based from all the reference images. In this section, we present the results of the AUC of each reference image and detector plotted according to the month in which the reference image was acquired regardless of the year. That is, all the images acquired in March between 2017 and 2023 are all grouped together as shown in the box plot in Fig. 6. From the analysis of the plot, there are observable variabilities of the AUC across the year and within the months for all detectors.

Detectors: The detectors *Rat1*, *Rat2*, *RatVH* and *RatVV* are observed to be less sensitive to the reference image selection while difference based are considered to be generally poor detectors. The ratio based detectors are consistently high throughout the year an display minimal annual or intra-month variability.

Reference image: The assessment of variability of the AUC of the reference image shows monthly variability and intra-monthly variability. For all detectors, there is least variability in the AUC from images acquired in March. March is also recorded to have the highest AUC for most detectors.

In summary, the analysis of the effect of selecting the reference image shows that the accuracy of flood detection is greatly influenced by the reference image selection. Images acquired in March have highest AUC. Generally, the images acquired in March will give the best detection of floods regardless of the year in which they were acquired. *Rat1*, *Rat2*, *RatVV*, and *RatVH* detectors are least sensitive to reference

This work is licensed under a Creative Commons Attribution 4.0 License. For more information, see https://creativecommons.org/licenses/by/4.0/

This article has been accepted for publication in IEEE Journal of Selected Topics in Applied Earth Observations and Remote Sensing. This is the author's version which has not been fully edited and content may change prior to final publication. Citation information: DOI 10.1109/JSTARS.2025.3628450

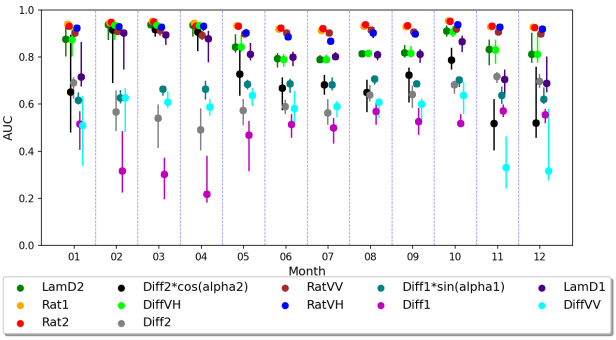

Fig. 6. Boxplot of the monthly variability of AUC using different reference (including from different years) images in Frame 1. The plots are grouped in months where each month in the box plot contains AUC values from which reference images within the month lie in.

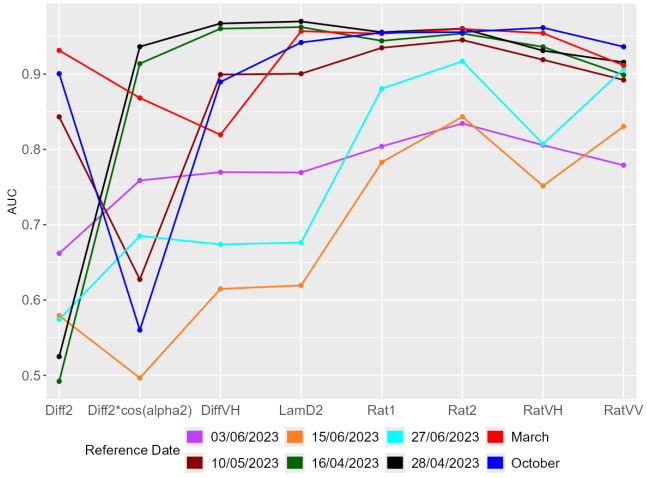

Fig. 7. AUC from the analysis of Frame 1 when different reference images are used. The detectors are plotted on the X-axis while the performance in each metric analysed on the Y-axis. The different colours represent the dates of reference images used in the analysis. March(red) and October(blue) represent a mean of all images in each month across all the years with data.

image selection. The backscattering intensity ratio *RatVV* and *RatVH* have almost comparable performance to polarimetric ratio-based detectors *Rat1* and *Rat2*. The box plot analysis of PD, PF, accuracy and F1-score FOR frames 1 and 2 display the same characteristics as the AUC plot. Similarly, the AUC plot for frame 2 shows the same characteristics. For this reason, they have been omitted.

E. Single or Average of Images for Reference

In the last section, we established that the images acquired in March from all years were have better performance in separating flood from non-flood areas. In this section we are presenting the results of comparison where we averaged all the images in March for all the years and used the mean image as reference against single images acquired before and after flood. In addition to mean of March, mean of October were also tested as shown in Fig. 7.

The analysis of frame 1 data shows that the second last image acquired 24 days (2023-04-28) before the flood was best in separating flooded areas for three difference based tested detectors (*LamD2*, *Diff2*cos(alpha2)* and *DiffVH*). The third image before a flood 2023-04-16 had almost similar performance although slightly lower. The mean of March image was best in three detectors *Rat2*, *Rat1*, and *Diff2*. Three reference images acquired after the flood (2023-06-03, 2023-06-15 and 2023-06-27) and the image just before the flood (2023-05-10) had the lowest AUC compared to the 2023-04-16 and mean images.

PF: Interestingly, when considering PF rates (results not shown here), the mean of images acquired in March had the lowest PF rates in *Rat1* and *Rat2*, had second lowest PF rate on *LamD2* and had the third lowest PF rate after the 2023-04-28 and 2023-04-16 images for *Diff2*, *Diff2*cos(alpha2)* and *DiffVH*. The other reference and detectors images had higher PF rates. The results of PD, PF, and accuracy depict similar trend and have been ormited.

In summary, the results show that the image acquired right before the flood does not necessarily give the best detection of floods. The second and third image before may be the best single reference image. An interesting observation is that the mean of the images of the month gives the lowest PF rates and almost comparable or better accuracy, and AUC when using the *Rat1* and *Rat2* compared to the best reference. *Rat1* and *Rat2* detectors give the lowest PF rates. When accurately selected, single image reference give low PF than the mean of month images when using the ratio of backscatter intensity *RatVV* an *RatVH*. The after-flood images are not the best to use as reference images. Selecting the right reference image will give the best accuracy of detection and the least PF rates. In general, averaging images over a month reduces PF rates and achieves almost comparable performance as the best reference image. The key finding is that it may be advantageous to use the mean of images over a month instead of a single image as reference, when there is no certainty on which date is best used as reference image. The analysis of Frame 2 shows similar results to Frame 1 and is therefore omitted.

F. Performance of Mean of March against best Single Image for all detectors

The previous section established that the use of mean of a month improves performance of detection of floods in most detectors. We also established that the best single image to be used as reference is acquired a month before the flood, therefore, in this section we are comparing the best single reference image (2023-04-28) for frame 1 against the mean of March and extent the analysis to all detectors including those considered poor detectors. There are differences in performance as shown in Fig. 8. In general, there are instances where detection performance improved, decreased or remain the same when using the mean of March as reference. Five detectors that recorded an improvement in AUC are *Diff1*, *Diff2*, *Diff1*sin(alpha1)*, *DiffVV*, and *RatVH*. The most improved detector was *Diff1* increasing by 0.72 while the least improved (*RatVH*) increasing by 0.02. Four detectors which decreased in their recorded AUC were *LamD2*, *Diff2*cos(alpha2)*, *RatVV*, and *DiffVH* with the largest decrease being by 0.12 (*Diff2*cos(alpha2)*)

This work is licensed under a Creative Commons Attribution 4.0 License. For more information, see https://creativecommons.org/licenses/by/4.0/

This article has been accepted for publication in IEEE Journal of Selected Topics in Applied Earth Observations and Remote Sensing. This is the author's version which has not been fully edited and content may change prior to final publication. Citation information: DOI 10.1109/JSTARS.2025.3628450

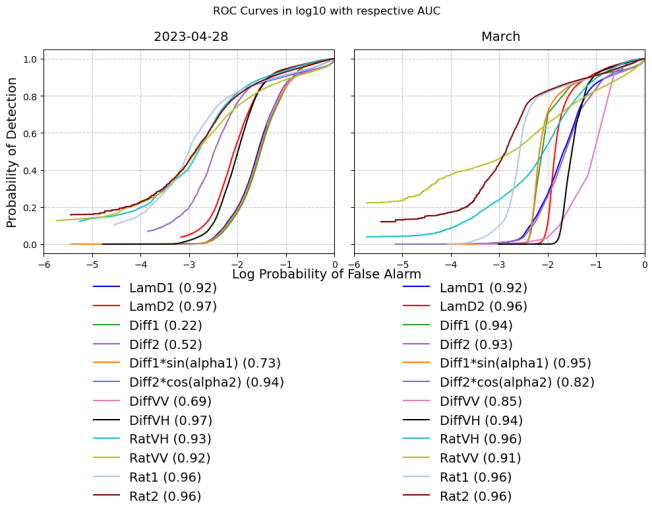

Fig. 8. The ROC curve plot of log PF against PD showing the performance of detector. The AUC for each detector is given next to the detector in the legend. The sub-plots represent the different reference images used for flood detection in Frame 1.

and least by 0.01 (*RatVV* & *LamD2*). Other detector did not record any change. In summary, there is an improvement in performance of detection for most detectors when using the mean of March images as reference with few detectors showing reduced performance.

G. Overall Detection Performance

In this section, we rank the detectors based on their performance using the overall performance indicator described in section II-C6. The outputs of the combination are shown in Table V where performance indicators from Frames 1 and 2 were combined. The analysis shows that the *Rat2* and *RatVV* are the best ranked detectors. The third detector is *Rat1*. *RatVH* is the fourth detector with over 80% performance. All other detectors have les than 80% performance. Interestingly, two detectors ranked second last (*DiffVV*) and last (*Diff1*) have performance below 70%. In summary, the analysis of the performance detectors shows that the ratio-based detectors perform better than difference-based detectors. The best performing detectors are polarimetric ratio-based change detectors (*Rat1* and *Rat2*) and backscatter intensity ratio (*RatVV* and *RatVH*) due to low PF rates. The difference in the *VV* polarisation channel (*DiffVV*) is a poor flood detector.

H. Testing on an Independent Dataset

1) Imola Frame 3: When we plot frame 3 data which has different acquisition characteristics as the first 2 and acquired 4 days later, there are some interesting observations. When we consider accuracy of detection, the mean of March images improved the accuracy by at least 2% for all detectors except for the *RatVH* when compared to the 2023-04-21 image and by up to 10% for detectors earlier considered poor (results omitted in the Fig. 9). It is also interesting to observe that all detectors have an almost identical accuracy when using the mean of March images with a maximum difference of 3% between the

TABLE V
RANK OF DETECTORS USING THEIR OVERALL PERFORMANCE

Rank	Detector	Overall Performance
1	*Rat2*	0.854
2	*RatVV*	0.849
3	*Rat1*	0.842
4	*RatVH*	0.823
5	*LamD2*	0.777
6	*DiffVH*	0.754
7	*Diff2*cos(alpha2)*	0.750
8	*LamD1*	0.739
9	*Diff2*	0.738
10	*Diff1*sin(alpha1)*	0.721
11	*DiffVV*	0.686
12	*Diff1*	0.683

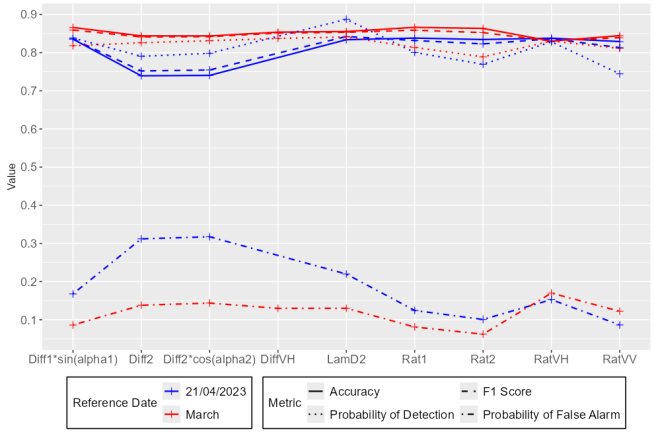

Fig. 9. Plot showing validation results when analysis of Frame 3 is carried out. The different colours represent date of reference (red-mean of March, blue- 2023-04-21) while the symbol represents the parameter analysed

highest and lowest accurate detector from the six selected. A closer look at the PF rates also shows another interesting and observable difference across all detectors except the *RatVV* and *RatVH*. The mean of March images gives the lowest PF rates in the detectors except for *RatVV* and *RatVH* which had a lower PF rate from the 2023-04-21 image. On the other hand, the *RatVV*, *Rat1*, *Rat2* and *Diff1*sin(alpha1)* have the least PF rates of less than 10%. When using the 2023-04-21 image, *RatVV*, *Rat1* and *Rat2* have the lowest PF rates between 8% and 15% higher than the mean of March image. All other detectors have PF rates between 15% and 35%.

In summary, the use of the mean of March image as reference for flood change detection generally leads to significant and substantial reductions in false alarms (PF). The mean image also improves the accuracy of the detection of floods and almost equalises the performance of all detectors to have the same accuracy. This can be very useful in the cases were selecting one single image is not clear. We have also established that the polarimetric change detector of *Rat1* and *Rat2* are the best detectors with low PF rates. These results confirm the performance of the mean of March images as a reference is better than the single image references.

This work is licensed under a Creative Commons Attribution 4.0 License. For more information, see https://creativecommons.org/licenses/by/4.0/

This article has been accepted for publication in IEEE Journal of Selected Topics in Applied Earth Observations and Remote Sensing. This is the author's version which has not been fully edited and content may change prior to final publication. Citation information: DOI 10.1109/JSTARS.2025.3628450

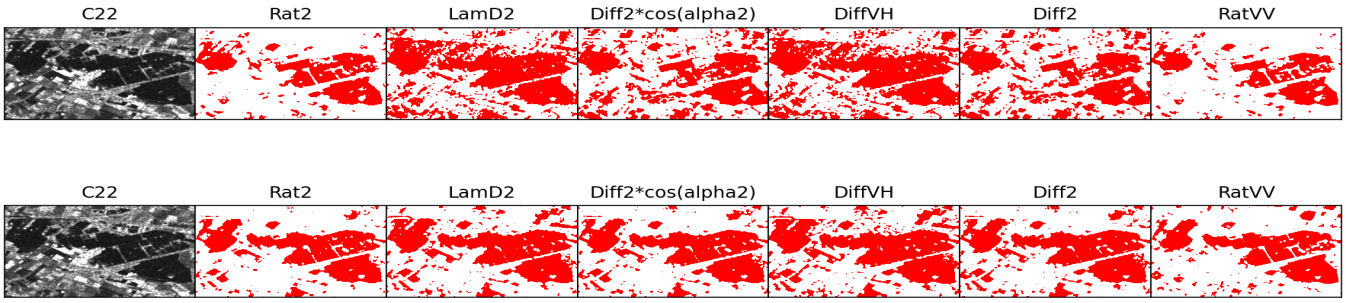

Fig. 10. Plot of a snippet of a flooded area on 2023-05-27 (left) and visual representation of how each detector predicted the flooded areas (red). The first sub-plot on the left is the C_{22} element of the area predicted. The top tiles represent results from change detection using the 2023-04-21 image as the reference image. Bottom tiles represent results from change detection using the mean of all March images as reference

2) Visualising Detector predictions: The results of detection when the best single reference image 2023-04-21 (month before flooding) and mean of a month (March) are shown in Fig. 10 from frame 3. Rat2 seems to be detecting floods better than any other detector. This is evident by how the areas flooded have been isolated. RatVV detector is also good at isolating flooded areas. The mean of March reference image seems to be more realistic when comparing all detectors. The 2023-04-21 image shows over-prediction in some areas across most detectors. *DiffVH* seems to have the highest over predicted areas (i.e. false alarms).

3) Forth Catchment, Scotland: In this section, we present the application of the *Rat2* detector over an area representing a different flood event in a catchment in Scotland. The detector was applied on SAR data acquired on 2023-10-08. The reference image in this case was mean of September images. September was selected in Scotland because like Imola, Italy, most land parcels have been cleared and are ploughed in preparation for the planting season. The results in Fig. 11 represents the flood extent map derived from the detector and compared against the product of CEMS. The results show that approximately 6,582 ha (441,514 pixels) of flooded area was classified as flooded from *Rat2* compared with 1,907.08 Ha derived from the CEMS. The *Rat2* result is before the application of any post-processing unlike the CEMS derived flood extent. The visual inspection of the flood extent map shows significant agreement between the two products along areas that are flooded. This result demonstrates the potential application of the detector in a different environment which is a temperate climate like Emilia-Romagna region.

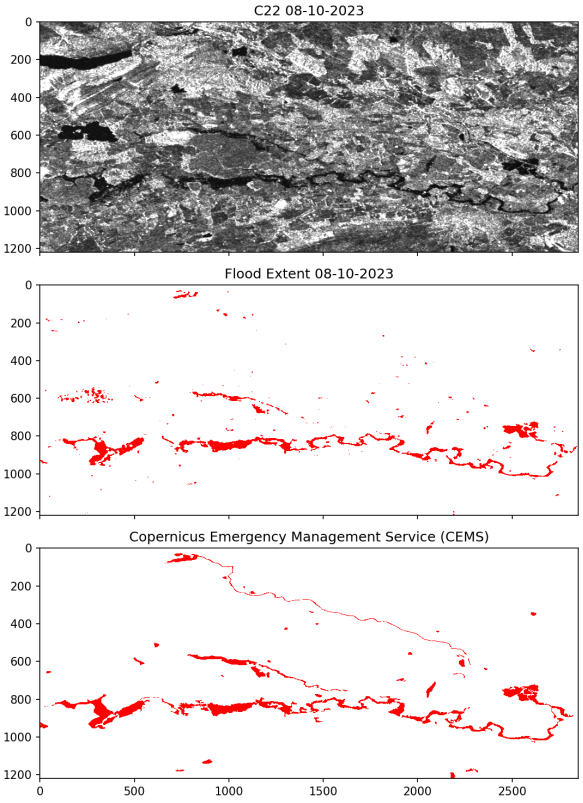

Fig. 11. Flood extent maps showing areas flooded in the Forth Catchment on the 08/10/2023. The tile on the top is the product of application of the *Rat2* detector and the mean of September images as reference. The tile at the bottom is a plot of a flood extent derived by the Copernicus Emergency Management Service after the activation of a chatter following the flood event.

I. Estimated Flood Inundation Extents on 2023-05-22, 2023-05-23, and 2023-05-27 in Imola

In this section, we are presenting the final flood map derived after applying the best detector which is *Rat2* and the mean of threshold with the highest accuracy and lest PF rates for Frame 1 and 2 for all dates. The results are presented as binary maps plotted with corresponding C_{22} elements (*VH* intensity) as shown in Fig. 12. The flood extent derived from the data analysis for 2023-05-22 (Frame 1) shows that approximately 9,980 ha (380,400 pixels) of land were flooded. On 2023-05-23, approximately 14,236 ha (542,400 pixels) were flooded from the analysis of frame 2. Frame 3 had approximately 6,710 ha (255,750 pixels) of area classified as flooded. It is important to note that this is only for the frame analysed and not for the entire SAR scene and the results presented have not been post-processed.

This work is licensed under a Creative Commons Attribution 4.0 License. For more information, see https://creativecommons.org/licenses/by/4.0/

This article has been accepted for publication in IEEE Journal of Selected Topics in Applied Earth Observations and Remote Sensing. This is the author's version which has not been fully edited and content may change prior to final publication. Citation information: DOI 10.1109/JSTARS.2025.3628450

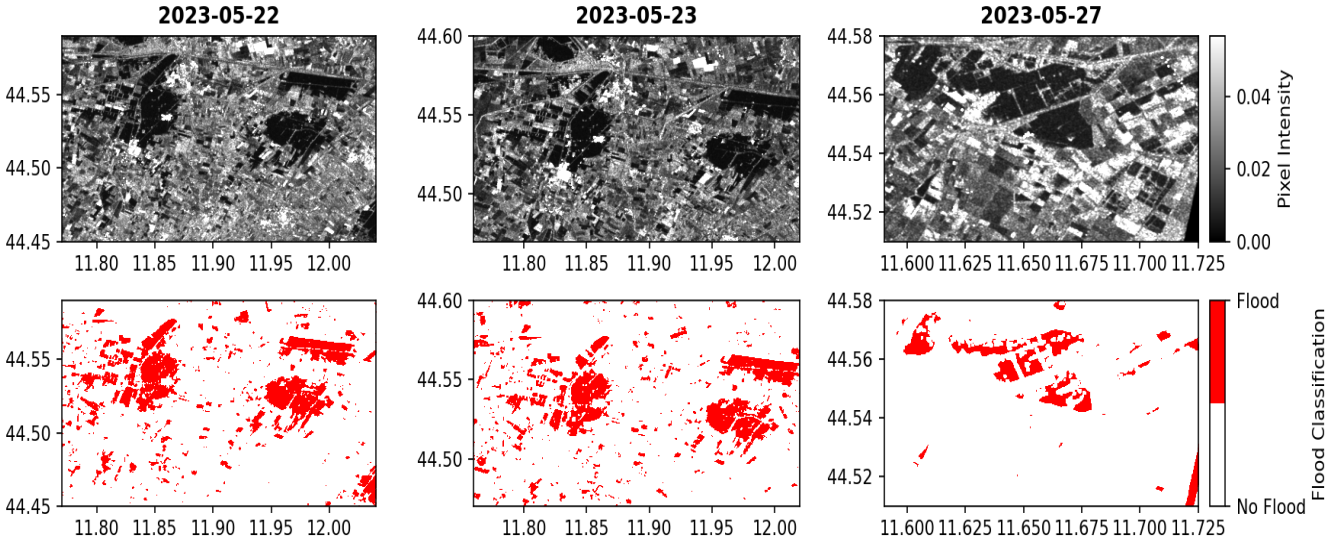

Fig. 12. Flood extent map derived from the data on the 2023-05-22, 2023-05-23, and 2023-05-27 images using the *Rat2* detector. The tile on top is the C_{22} element of the covariance matrix. Bottom is the binary flood extent derived plotted for a selected area of the SAR frame analysed. The binary result is without any post-processing.

IV. Discussion

In this article, we have applied polarimetric change detection methods of OPDiff and OPRatio for the first time to map the areas inundated by floods. We have also applied time series data available to determine the best reference image to be used in the change detection. We established that polarimetric change detection method *Rat2* of the OpRatio detector is the best at mapping open floods. This method has the highest AUC which measures classifier performance [41]. *Rat2* also has the highest threshold depended accuracy, PF and F1-score. This detector is based on the second eigenvalue from the dual-pol data. The other ratio based detectors *Rat1* and backscatter intensity (*RatVV* & *RatVH*) were better at detecting floods compared to difference based detectors such as difference in intensity of *VH* and *VV* polarization. We also established that the second eigenvalue of the Cloude-Pottier decomposition is more accurate at mapping floods than the difference in intensity of *VH*. When comparing two images, and in agricultural areas, the second eigenvalue captures information about depolarizing scatterers, like vegetation. A flood image dominated by specular reflection from water leads to a lower scattering power in the second eigenvalue which was stronger in the image before floods. The first eigenvector is more sensitive to changes, making it prone to false alarms. We also found that *VH* intensity differences have significantly lower accuracy than polarimetric detectors (*Rat1*, *Rat2*) and backscatter ratios (*RatVV*, *RatVH*), with high false alarms. *DiffVV* was the poorest detector for mapping open floods, consistent with findings that *VV* polarization is sensitive to surface roughness [24]. Previous researchers established that *DiffVH* outperforms *DiffVV* [42], [43]. We have established that in general, the ratio based detectors were more accurate and robust than the difference between based detectors. These detectors recorded higher accuracies, lower false alarm rates and less sensitivity.

We applied a semi-automated technique to select the best threshold value that gives the highest accuracy and least false alarm when estimating the threshold-dependent parameters (PD, PF, accuracy and F1-score). The technique is dependent on the optical image used to evaluate the effectiveness. However, in a flood event, optical images are not readily available, in the absence of this, other thresholding methods can be applied to the image after change detection such as Otsu [19], KI [20]. This is because we have established the detection method that gives the largest separation distance between flood and non-flood value. Selecting the correct reference image is crucial for accurate flood mapping. Using an incorrect reference can increase false alarms and introduce uncertainty [18]. While prior studies applied the last image before a flood as the reference [42], our research found this does not always ensure accurate detection due to potential saturation and inundation. In our study area, our analysis shows that using the second or third image before a flood is better, typically taken a month before the event. Unexpectedly, we found that using the mean of all images in March across years improved change detection. This study demonstrates that using a monthly mean image (e.g., March) as a reference minimizes false alarms compared to a single-date reference [44]. March in Italy is characterized by ploughed fields, which results in backscatter dominated by surface scattering and low soil moisture. We recommend using a mean image of a month with similar characteristics when reference image selection is uncertain, as it reduces noise and focuses on backscatter reduction. The downside is longer computation times, which can be mitigated with pre-processing in operational scenarios, though rapid environmental changes may complicate this approach.

We suggest that polarimetric change detection using the OpRatio (*Rat2*) is the best for identifying open floods. In the absence of polarimetric data, the *VV* backscatter ratio per-

This work is licensed under a Creative Commons Attribution 4.0 License. For more information, see https://creativecommons.org/licenses/by/4.0/

This article has been accepted for publication in IEEE Journal of Selected Topics in Applied Earth Observations and Remote Sensing. This is the author's version which has not been fully edited and content may change prior to final publication. Citation information: DOI 10.1109/JSTARS.2025.3628450

forms similarly. We also demonstrated a practical method for selecting the reference image, improving detection accuracy. Combining the suggested flood mapping method and reference image selection will reduce false alarms. Although the reference image selection and best detector were tested in Scotland resulting in comparable performance with established operational methods, we cannot confirm the performance of the methodology in other parts of the world besides Europe. Further studies in different regions are needed to understand the environmental factors influencing reference image selection. Since we assessed each index separately, future studies could explore ensemble decision frameworks (including machine learning ones) that integrate multiple indices (*Rat2*, *RatVV*, *Rat1*, *RatVH*), which may complement individual detector strengths and further reduce classification errors. This study focused on open flooded areas, so future work will explore how these methods perform in other flood scenarios, such as those involving inundated vegetation. Additionally, soil conditions influencing reference image selection were not examined. The processing time required for polarimetric data processing and reference images selection is longer compared to analysis of backscatter intensity only. Regarding the data used, the lack of the fully polarimetric data hinders the full quantification of the scattering mechanism. Despite this, Sentinel-1's global coverage, open-access policy and high temporal resolution makes it advantageous to use the data. For instance, with the current Sentinel-1 constellation, an average 58% of global flood events can be captured [45] with high accuracy offering high reliability in flood mapping. The polarimetric change detection methods have been previously applied in aquatic vegetation mapping [46], [47], crop monitoring [48], and plastic mapping [49] with over 80% accuracies demonstrating wide application.

V. Conclusion

In this study, we analysed timeseries SAR data from Imola, Italy, with a reference to a flood event in May 2023 to determine how to improve the accuracy of flood mapping while reducing false alarms. We utilised Sentinel-1 dual polarimetric data and applied polarimetric change detection methods of Optimisation of Power Difference and Optimisation of Power ratio. We also for the first time tested all historical images on record as reference image to determine the best reference image for flood mapping.

By using a monthly mean of Sentinel-1 images as the reference, we improved flood detection accuracy by over 3% and reduced false alarms by approximately 5% compared to conventional single-image methods. The Optimisation of power ratio detector achieved overall accuracies above 85% and false alarm rates below 10%. Furthermore, the results for a major flood event in Scotland were comparable to products from the Copernicus Emergency Management Service, demonstrating the operational potential of our approach. While the focus was on open water floods, the presented methodology lays the groundwork for future investigations into more challenging scenarios, such as flooding beneath vegetation canopies or in diverse climatic zones. This work addresses a critical challenge in SAR-based flood monitoring, offering a more reliable and accurate technique for reference image selection that can be readily integrated into operational emergency response systems.

Funding

This work was supported by the Natural Environment Research Council via an IAPETUS2 PhD studentship held by Isundwa Kasiti Felix [grant number NE/S007431/1] and by Scottish Environment Protection Agency.

References

[1] B. Merz, G. Blöschl, S. Vorogushyn, F. Dottori, J. C. J. H. Aerts, P. Bates, M. Bertola, M. Kemter, H. Kreibich, U. Lall, and E. Macdonald, "Causes, impacts and patterns of disastrous river floods," *Nature Reviews Earth & Environment*, vol. 2, no. 9, pp. 592-609, 2021. [Online]. Available: https://doi.org/10.1038/s43017-021-00195-3

[2] H. J. Fowler, G. Lenderink, A. F. Prein, S. Westra, R. P. Allan, N. Ban, R. Barbero, P. Berg, S. Blenkinsop, and H. X. Do, "Anthropogenic intensification of short-duration rainfall extremes," *Nature Reviews Earth & Environment*, vol. 2, no. 2, pp. 107–122, 2021.

[3] H. Tabari, "Climate change impact on flood and extreme precipitation increases with water availability," *Scientific Reports*, vol. 10, no. 1, p. 13768, 2020. [Online]. Available: https://doi.org/10.1038/s41598-020-70816-2

[4] R. B. Mudashiru, N. Sabtu, I. Abustan, and W. Balogun, "Flood hazard mapping methods: A review," *Journal of Hydrology*, vol. 603, p. 126846, 2021. [Online]. Available: https://www.sciencedirect.com/science/article/pii/S0022169421008969

[5] X. Wang and H. Xie, "A Review on Applications of Remote Sensing and Geographic Information Systems (GIS) in Water Resources and Flood Risk Management," 2018.

[6] F. Policelli, D. Slayback, B. Brakenridge, J. Nigro, A. Hubbard, B. Zaitchik, M. Carroll, and H. Jung, *The NASA Global Flood Mapping System*. Cham: Springer International Publishing, 2017, ch. 3, pp. 47–63. [Online]. Available: https://doi.org/10.1007/978\-3\-319\-43744\-6_3

[7] S. Chignell, R. Anderson, P. Evangelista, M. Laituri, and D. Merritt, "Multi-Temporal Independent Component Analysis and Landsat 8 for Delineating Maximum Extent of the 2013 Colorado Front Range Flood," *Remote Sensing*, vol. 7, no. 8, pp. 9822–9843, jul 2015. [Online]. Available: https://www.mdpi.com/2072-4292/7/8/9822

[8] H. Mehmood, C. Conway, and D. Perera, "Mapping of Flood Areas Using Landsat with Google Earth Engine Cloud Platform," 2021.

[9] I. Nandi, P. K. Srivastava, and K. Shah, "Floodplain Mapping through Support Vector Machine and Optical/Infrared Images from Landsat 8 OLI/TIRS Sensors: Case Study from Varanasi," *Water Resources Management*, vol. 31, no. 4, pp. 1157–1171, 2017. [Online]. Available: https://doi.org/10.1007/s11269-017-1568-y

[10] S. Li, D. Sun, M. D. Goldberg, B. Sjoberg, D. Santek, J. P. Hoffman, M. DeWeese, P. Restrepo, S. Lindsey, and E. Holloway, "Automatic near real-time flood detection using Suomi-NPP/VIIRS data," *Remote Sensing of Environment*, vol. 204, pp. 672–689, 2018. [Online]. Available: https://www.sciencedirect.com/science/article/pii/S0034425717304431

[11] P. Jain, B. Schoen-Phelan, and R. Ross, "Automatic flood detection in SentineI-2 images using deep convolutional neural networks," in *Proceedings of the 35th Annual ACM Symposium on Applied Computing*, ser. SAC '20. New York, NY, USA: Association for Computing Machinery, 2020, pp. 617–623. [Online]. Available: https://doi.org/10.1145/3341105.3374023

[12] I. Ilia, P. Tsangaratos, P. Tzampoglou, W. Chen, and H. Hong, "Flash flood susceptibility mapping using stacking ensemble machine learning models," *Geocarto International*, vol. 37, no. 27, pp. 15 010–15 036, dec 2022. [Online]. Available: https://doi.org/10.1080/10106049.2022.2093990

[13] A. Salvati, A. M. Nia, A. Salajegheh, K. Ghaderi, D. T. Asl, N. Al-Ansari, F. Solaimani, and J. J. Clague, "Flood susceptibility mapping using support vector regression and hyper-parameter optimization," *Journal of Flood Risk Management*, vol. 16, no. 4, p. e12920, dec 2023. [Online]. Available: https://doi.org/10.1111/jfr3.12920

This work is licensed under a Creative Commons Attribution 4.0 License. For more information, see https://creativecommons.org/licenses/by/4.0/

This article has been accepted for publication in IEEE Journal of Selected Topics in Applied Earth Observations and Remote Sensing. This is the author's version which has not been fully e
content may change prior to final publication. Citation information: DOI 10.1109/JSTARS.2025.3628450

[14] L. Ji, L. Zhang, and B. Wylie, "Analysis of Dynamic Thresholds for the Normalized Difference Water Index," *Photogrammetric Engineering & Remote Sensing*, vol. 75, pp. 1307–1317, nov 2009.

[15] B. Weintrit, K. Osińska-Skotak, and M. Pilarska, "Feasibility study of flood risk monitoring based on optical satellite data," *Miscellanea Geographica*, vol. 22, pp. 172–180, 2018. [Online]. Available: https://api.semanticscholar.org/CorpusID:134645025

[16] X. Shen, D. Wang, K. Mao, E. Anagnostou, and Y. Hong, "Inundation extent mapping by synthetic aperture radar: A review," *Remote Sensing*, vol. 11, no. 7, apr 2019. [Online]. Available: https://www.mdpi.com/2072-4292/11/7/879

[17] H.-Y. Liao and T.-H. Wen, "Extracting urban water bodies from high-resolution radar images: Measuring the urban surface morphology to control for radar's double-bounce effect," *International Journal of Applied Earth Observation and Geoinformation*, vol. 85, p. 102003, 2020. [Online]. Available: https://www.sciencedirect.com/science/article/pii/S0303243419306968

[18] L. Landuyt, A. V. Wesemael, G. J. . .-P. Schumann, R. Hostache, N. E. C. Verhoest, and F. M. B. V. Coillie, "Flood Mapping Based on Synthetic Aperture Radar: An Assessment of Established Approaches," *IEEE Transactions on Geoscience and Remote Sensing*, vol. 57, no. 2, pp. 722-739, 2019.

[19] N. Otsu, "A Threshold Selection Method from Gray-Level Histograms," *IEEE Transactions on Systems, Man, and Cybernetics*, vol. 9, no. 1, pp. 62–66, 1979.

[20] J. Kittler and J. Illingworth, "Minimum error thresholding," *Pattern Recognition*, vol. 19, no. 1, pp. 41-47, 1986. [Online]. Available: {https://www.sciencedirect.com/science/article/pii/0031320386900300}

[21] N. Gupta, S. Ari, and A. K. Mishra, "A novel unsupervised thresholding technique for landsat image change detection," *Proceedings of the Twelfth Indian Conference on Computer Vision, Graphics and Image Processing*, 2021. [Online]. Available: https://api.semanticscholar.org/CorpusID:245132804

[22] Y. Li, S. Martinis, S. Plank, and R. Ludwig, "An automatic change detection approach for rapid flood mapping in Sentinel-1 SAR data," *International Journal of Applied Earth Observation and Geoinformation*, vol. 73, pp. 123–135, 2018. [Online]. Available: https://www.sciencedirect.com/science/article/pii/S0303243418302782

[23] J. Zhao, M. Chini, P. Matgen, R. Hostache, R. Pelich, and W. Wagner, "An Automatic SAR-Based Change Detection Method for Generating Large-Scale Flood Data Records: The UK as a Test Case," in *IGARSS 2019 - 2019 IEEE International Geoscience and Remote Sensing Symposium*, 2019, pp. 6138–6141.

[24] P. Manjusree, L. Prasanna Kumar, C. M. Bhatt, G. S. Rao, and V. Bhanumurthy, "Optimization of threshold ranges for rapid flood inundation mapping by evaluating backscatter profiles of high incidence angle SAR images," *International Journal of Disaster Risk Science*, vol. 3, no. 2, pp. 113–122, 2012. [Online]. Available: https://doi.org/10.1007/s13753-012-0011-5

[25] R. Manavalan, Y. S. Rao, and B. Krishna Mohan, "Comparative flood area analysis of C-band VH, VV, and L-band HH polarizations SAR data," *International Journal of Remote Sensing*, vol. 38, no. 16, pp. 4645–4654, aug 2017. [Online]. Available: https://doi.org/10.1080/01431161.2017.1325534

[26] A. Adiba and F. Bioresita, "Sentinel-1 SAR Polarization Combinations for Flood Inundation Spatial Distribution Mapping (Case Study: South Kalimantan)," *IOP Conference Series: Earth and Environmental Science*, vol. 1127, 2023. [Online]. Available: https://api.semanticscholar.org/CorpusID:256052915

[27] T. W. Bekele, A. T. Haile, M. A. Trigg, and C. Walsh, "Evaluating a new method of remote sensing for flood mapping in the urban and peri-urban areas: Applied to Addis Ababa and the Akaki catchment in Ethiopia," *Natural Hazards Research*, 2022. [Online]. Available: https://api.semanticscholar.org/CorpusID:247573998

[28] M. Chini, A. Papastergios, L. Pulvirenti, N. Pierdicca, P. Matgen, and I. S. Parcharidis, "SAR coherence and polarimetric information for improving flood mapping," *2016 IEEE International Geoscience and Remote Sensing Symposium (IGARSS)*, pp. 7577–7580, 2016. [Online]. Available: https://api.semanticscholar.org/CorpusID:20931659

[29] L. G. Pillai and D. R. J. Dolly, "Flood detection using SAR images: A review," *PROCEEDINGS OF THE INTERNATIONAL CONFERENCE ON RESEARCH ADVANCES IN ENGINEERING AND TECHNOLOGY - ITechCET 2022*, 2024. [Online]. Available: https://api.semanticscholar.org/CorpusID:267354432

[30] B. Bauer-Marschallinger, S. Cao, M. E. Tupas, F. Roth, C. Navacchi, T. Melzer, V. Freeman, and W. Wagner, "Satellite-Based Flood Mapping through Bayesian Inference from a Sentinel-1 SAR Datacube," *Remote Sensing*, vol. 14, no. 15, 2022. [Online]. Available: https://www.mdpi.com/2072-4292/14/15/3673

[31] M. Chini, R. Hostache, L. Giustarini, and P. Matgen, "A Hierarchical Split-Based Approach for Parametric Thresholding of SAR Images: Flood Inundation as a Test Case," *IEEE Transactions on Geoscience and Remote Sensing*, vol. 55, no. 12, pp. 6975–6988, 2017.

[32] S. Martinis, J. Kersten, and A. Twele, "A fully automated TerraSAR-X based flood service," *ISPRS Journal of Photogrammetry and Remote Sensing*, vol. 104, pp. 203–212, 2015. [Online]. Available: https://www.sciencedirect.com/science/article/pii/S0924271614001981

[33] D. Ghiglione and S. Bettiza, "Italy floods leave 13 dead and force 13,000 from their homes," 2023. [Online]. Available: https://www.bbc.co.uk/news/world-europe-65632655

[34] M. Kendon, "Exceptional rainfall in Scotland, 6 to 7 October 2023," Met Office National Climate Information Centre, Tech. Rep., 2023. [Online]. Available: {https://www.metoffice.gov.uk/binaries/content/assets/metofficegovuk/\\pdf/weather/learn\-about/uk\-pastevents/interesting/2023/\\2023_07_scotland_rain.pdf}

[35] R. Piantanida, G. Hajduch, and J. Poullaouec, "Sentinel-1 level 1 detailed algorithm definition," *ESA, techreport SEN-TN-52-7445*, 2016.

[36] P. L. PBC, "Planet Application Program Interface: In Space for Life on Earth," 2023. [Online]. Available: https://api.planet.com

[37] I. H. Woodhouse, *Introduction to microwave remote sensing*. CRC Press, 2017. [Online]. Available: https://books.google.co.uk/books?id=9x8uDwAAQBAJ

[38] S. R. Cloude and E. Pottier, "A review of target decomposition theorems in radar polarimetry," *IEEE Transactions on Geoscience and Remote Sensing*, vol. 34, no. 2, pp. 498–518, 1996.

[39] A. Marino and M. Nannini, "Signal Models for Changes in Polarimetric SAR Data," *IEEE Transactions on Geoscience and Remote Sensing*, vol. 60, pp. 1–18, 2022.

[40] A. Marino and I. Hajnsek, "A change detector based on an optimization with polarimetric SAR imagery," *IEEE Transactions on Geoscience and Remote Sensing*, vol. 52, no. 8, pp. 4781–4798, 2014.

[41] T. Fawcett, "Introduction to ROC analysis," *Pattern Recognition Letters*, vol. 27, pp. 861–874, jun 2006.

[42] F. Carreño Conde and M. De Mata Muñoz, "Flood Monitoring Based on the Study of Sentinel1 SAR Images: The Ebro River Case Study," 2019.

[43] A. Risling, S. Lindersson, and L. Brandimarte, "A comparison of global flood models using Sentinel-1 and a change detection approach," *Natural Hazards*, 2024. [Online]. Available: https://www.scopus.com/inward/record.uri?eid\=2\-s2.0\-85192526255\&doi\=10.1007\%2Fs11069\-024\-06629\-7\&partnerID\=40\&md5\=98ccc607d8ce2b5f1b886df5958540c0

[44] S. Schlaffer, P. Matgen, M. Hollaus, and W. Wagner, "Flood detection from multi-temporal SAR data using harmonic analysis and change detection," *International Journal of Applied Earth Observation and Geoinformation*, vol. 38, pp. 15–24, 2015. [Online]. Available: https://www.sciencedirect.com/science/article/pii/S0303243414002645

[45] A. Tarpanelli, A. C. Mondini, and S. Camici, "Effectiveness of sentinel-1 and sentinel-2 for flood detection assessment in europe," *Natural Hazards and Earth System Sciences*, vol. 22, no. 8, pp. 2473–2489, 2022. [Online]. Available: https://nhess.copernicus.org/articles/22/2473/2022/

[46] I. K. Felix, M. Armando, M. D. Simpson, A. Vahid, T. S. F. Silva, A. Datta, P. G. Nagendra, G. Pranuthi, and R. Srikanth, "Mapping and Monitoring Of Water Hyacinth In Lake Victoria Using Polarimetric Radar Data," *IEEE Journal of Selected Topics in Applied Earth Observations and Remote Sensing*, pp. 1–11, 2024.

[47] M. D. Simpson, V. Akbari, A. Marino, G. N. Prabhu, D. Bhowmik, S. Rupavatharam, A. Datta, A. Kleczkowski, J. A. R. P. Sujeetha, G. G. Anantrao, V. K. Poduvattil, S. Kumar, S. Maharaj, and P. D. Hunter, "Detecting water hyacinth infestation in kuttanad, india, using dual-pol sentinel-1 sar imagery," *Remote Sensing*, vol. 14, no. 12, 2022. [Online]. Available: https://www.mdpi.com/2072-4292/14/12/2845

[48] C. Silva-Perez, A. Marino, J. M. Lopez-Sanchez, and I. Cameron, "Multitemporal Polarimetric SAR Change Detection for Crop Monitoring and Crop Type Classification," *IEEE Journal of Selected Topics in Applied Earth Observations and Remote Sensing*, vol. 14, pp. 12 361–12 374, 2021. [Online]. Available: https://ieeexplore.ieee.org/document/9625782/

[49] M. D. Simpson, A. Marino, P. de Maagt, E. Gandini, P. Hunter, E. Spyrakos, A. Tyler, and T. Telfer, "Monitoring of plastic islands in river environment using sentinel-1 sar data," *Remote Sensing*, vol. 14, no. 18, 2022. [Online]. Available: https://www.mdpi.com/2072-4292/14/18/4473

This work is licensed under a Creative Commons Attribution 4.0 License. For more information, see https://creativecommons.org/licenses/by/4.0/

This article has been accepted for publication in IEEE Journal of Selected Topics in Applied Earth Observations and Remote Sensing. This is the author's version which has not been fully e
content may change prior to final publication. Citation information: DOI 10.1109/JSTARS.2025.3628450

Isundwa Kasiti Felix (Student Member, IEEE) received the B.Sc. degree in earth sciences (Hydrology and Water Resources Management option) from Maseno University, Maseno, Kenya, in 2013, and the M.Sc. degree in water policy from the Institute of Water and Energy Sciences, Pan African University, Tlemcen, Algeria, in 2018. He is currently working toward the Ph.D. degree in mapping and monitoring floods using SAR Polarimetry with the Faculty of Natural Sciences, University of Stirling, Stirling, U.K.

From 2014 to 2016, he was a Consulting Hydrologist. He later joined SERVIR Eastern and Southern Africa project with the Regional Centre for Mapping of Resources for Development, Nairobi, Kenya, in 2019, as an assistant hydrologist.

Armando Marino (Member, IEEE) received the M.Sc. degree in telecommunication engineering from the Universita' di Napoli "Federico II", Naples, Italy, in 2006.

In 2006, he joined the High Frequency and Radar Systems Department, German Aerospace Centre, Oberpfaffenhofen, Germany, where he developed his M.Sc. thesis. He received a PhD. in polarimetric SAR interferometry from the School of Geosciences, University of Edinburgh, Edinburgh, U.K. in 2011. From March 2011 to October 2011,he was with the University of Alicante, Institute of Computing Research, Spain. From December 2011 to May 2015, he was a Postdoctoral Researcher and Lecturer with ETH Zurich, Institute of Environmental Engineering, Switzerland. From June 2015, he was a Lecturer with the School of Engineering and Innovation, Open University, Milton Keynes, U.K. Since May 2018 he has been an Associate Professor at the University of Stirling, Faculty of Natural Sciences, Stirling, UK.

Thiago S. F. Silva received the B.Sc. degree in biology from University of Rio Grande do Norte, Natal, Brazil, in 2002, the M.Sc. degree in remote sensing from the National Institute for Space Research (INPE), São Paulo, Brazil, in 2004, and the Ph.D. degree in physical geography from the University of Victoria, Victoria, BC, Canada, in 2009.

He worked then as a Researcher with the University of California Santa Barbara, Santa Barbara, CA, USA, in 2010, and INPE from 2011 to 2013. He then joined with the Geography Department, São Paulo State University, São Paulo, as an Assistant Professor from 2013 to 2019. Since 2019, he has been a Senior Lecturer with the Faculty of Natural Sciences, University of Stirling, Stirling, U.K. His research interests include ecology, geoscience, and data science to understand how global ecosystems are being affected by the global climatic and biodiversity crises.

This work is licensed under a Creative Commons Attribution 4.0 License. For more information, see https://creativecommons.org/licenses/by/4.0/